

Pseudomorphic Transformation of Interpenetrated Prussian Blue Analogs into Defective Nickel Iron Selenides for Enhanced Electrochemical and Photo-Electrochemical Water Splitting

Gamze Yilmaz, Chuan Fu Tan, Yee-Fun Lim, and Ghim Wei Ho*

A significant methodology gap remains in the construction of advanced electrocatalysts, which has collaborative defective functionalities and structural coherence that maximizes electrochemical redox activity, electrical conductivity, and mass transport characteristics. Here, a coordinative self-templated pseudomorphic transformation of an interpenetrated metal organic compound network is conceptualized into a defect-rich porous framework that delivers highly reactive and durable photo(electro)chemical energy conversion functionalities. The coordinative-template approach enables previously inaccessible synthesis routes to rationally accomplish an interconnected porous conductive network at the microscopic level, while exposing copious unsaturated reactive sites at the atomic level without electronic or structural integrity trade-offs. Consequently, porous framework, interconnected motifs, and engineered defects endow remarkable electrocatalytic hydrogen evolution reaction and oxygen evolution reaction activity due to intrinsically improved turnover frequency, electrochemical surface area, and charge transfer. Moreover, when the hybrid is coupled with a silicon photocathode for solar-driven water splitting, it enables photon assisted redox reactions, improved charge separation, and enhanced carrier transport via the built-in heterojunction and additive co-catalyst functionality, leading to a promising photo(electro)chemical hydrogen generation performance. This work signifies a viable and generic approach to prepare other functional interconnected metal organic coordinated compounds, which can be exploited for diverse energy storage, conversion, or environmental applications.

modulation owing to their diversity and highly anisotropic nanostructures. An ingenious strategy of atomic level structural engineering involves reconstruction of the atomic lattice in response to a subtle distortion or symmetry breakage. This concept uncovers not only a new atomic arrangement but also an electronic modulation due to adventitious crystal disorder/deformation, thus introduces novel physical, chemical, and electronic properties. Theoretical calculations and experimental studies have demonstrated that nanostructural disorder/deformation breaks the electronic neutrality of the crystal framework, creates unsaturated atomic sites, and tunes the surface adsorption energies of reaction intermediates, thereby enabling an effectual manipulation of the electrocatalytic activity.^[1] The most prominent approach to atomic level structural engineering is defect generation through heteroatom doping, vacancy creation, stacking fault/twin boundary/dislocation formation, and grain boundary-rich surface design.^[1b,2] Point defects (anion/cation vacancies) have generally shown promising activity triggering functionalities in electrocatalysts despite the frequent use of energy-intensive and cor-

rosive chemical/physical treatments (e.g., plasma-treatment and NaBH₄). However, in some cases, detrimental electrocatalytic performance has been also observed due to poor defect formation controllability and electronic conductivity decrease, mostly in perovskites.^[3] Lattice defect (e.g., dislocations, stepped surfaces, grain boundaries, twin boundaries), on the other hand, is an extended bulk imperfectness generally induced by stress. It boosts the catalytic activity by introducing excess unsaturated atomic sites in the form of enriched grain boundaries and edges, thus presenting an augmented effective catalytic active surface area compared to point defects.^[4] Though lattice defects naturally emanate in polycrystalline materials during crystal growth, they are mostly embedded in the bulk rather than being surfaced and exposed, thus making reactant accessibility difficult, specifically for less porous types. In view of the methodological gaps, synthesizing discrete nanosized transition metal

1. Introduction

Radical improvement in catalytic activity of transition metal derivatives is attainable via systematic structural and electronic

Dr. G. Yilmaz, C. F. Tan, Prof. G. W. Ho
Department of Electrical and Computer Engineering
National University of Singapore
4 Engineering Drive 3, 117583 Singapore, Singapore
E-mail: elehgw@nus.edu.sg

Dr. Y.-F. Lim, Prof. G. W. Ho
Institute of Materials Research and Engineering
A*STAR (Agency for Science, Technology and Research)
2 Fusionopolis Way, Innovis, 138634 Singapore, Singapore

 The ORCID identification number(s) for the author(s) of this article can be found under <https://doi.org/10.1002/aenm.201802983>.

DOI: 10.1002/aenm.201802983

derivative crystallites could render surface with abundant surface defect sites, yet other issues like agglomeration and active site blockage are often unavoidable during the electrocatalyst preparation, which leads to nonoptimal chemical interaction and ion diffusivity. Hence, incorporating abundant lattice defects into functional transition metal derivative crystal structures with exceptional accessibility, homogeneity, and dispersity is of paramount importance on account of unveiling the overwhelming richness of electrochemically stable and active sites. Specifically, creating a synergy between defective functionalities while maintaining structural coherence can, in turn, underpin remarkably improved reactivity, conductivity, and mass transfer properties.^[5] In this regard, microscopic level structural engineering could offer viable strategies to induce the structural coherence with favorable topological and electrical properties, such as improved electrical conductivity, charge mobility, and surface area.^[6] For example, it is possible to synthesize 3D network of transition metal derivative crystallites in carbon or polymeric skeleton with high structural integrity and uniformity.^[7] However, these crystallites are mostly discrete in the network and wrapped by the skeleton atoms rather than constructing a 3D fully interconnected architecture, resulting in a greatly limited electrocatalytic activity. Therefore, exposing accessible atomic-scale defective functionalities to the reaction medium via a rational microscopic-scale structural engineering strategy becomes a critical factor determining the electrocatalytic performance. On the basis of these premises, development of an effective approach which enables introduction of abundant surface lattice defects while preserving well-ordered interconnected 3D electrocatalyst structure is paramount yet remains challenging for electrocatalysis domain.

Herein, we conceptualized a coordinative self-templated approach to enable the preparation of 3D interpenetrating hierarchical nanoarchitectures directed by carbonate hydroxide motifs, followed by a thermal selenization to obtain porous, interconnected transition metal selenide heterostructures elaborated with defects. Sacrificial metal organic coordination compound (nickel iron Prussian blue analog (NiFe-PBA)) and nickel carbonate hydroxide (NiCH) templates are explicitly exploited to accomplish in situ defect and pore generation leveraging on the high stress inducing thermal decomposition of the nickel carbonate hydroxide during pseudomorphic selenization into nickel iron selenide hybrid (NiFeSe@NiSe|O@CC). The resulting structure possesses an interconnected porous conductive network at the microscopic level, while exposing large fraction of reactive crystal boundaries edge sites at the atomic level. Detailed electrochemical analysis reveals superior electrochemical and photo(electro)chemical (PEC) water splitting performance of the NiFeSe@NiSe|O@CC. It exhibits a highly efficient and stable electrocatalytic activity toward hydrogen evolution reaction (HER) and oxygen evolution reaction (OER) as well as overall water splitting in alkaline media with low overpotentials and remarkable stabilities. When coupled with p-type silicon for PEC water splitting, it can also significantly enhance hydrogen production performance by virtue of the established heterojunction and cocatalytic features. This work introduces a well-engineered nanostructured material that accounts both physically and electrochemically favorable structure, which can be employed in various catalytic applications.

It also highlights a generic coordinative-template synthesis strategy, allowing preparation of other interconnected metal organic coordination compounds, which may be exploited for diverse potential applications in energy storage, conversion, or environmental purposes.

2. Results and Discussion

3D interpenetrating hierarchical nanoarchitectures are prepared through a novel coordinative-template approach, in which metal-organic coordination compounds (MOCCs), such as PBAs or zeolitic imidazolate frameworks (ZIFs), are directly coordinated and grown on carbonate hydroxide nanosheet templates. As illustrated in Figure 1a and Figure S1 (Supporting Information), in a typical preparation process, first, NiCH is prepared on a flexible carbon fiber substrate (denoted as NiCH@CC) as a coordinative self-template by a facile hydrothermal method (Figure S2, Supporting Information).^[8] NiFe-PBA nanocubes are then readily synthesized and anchored on the NiCH@CC nanosheets by a kinetically controlled room-temperature crystallization process (denoted as NiFe-PBA@NiCH@CC).^[4a] Finally, NiFeSe@NiSe|O@CC is obtained by exposing the as-prepared NiFe-PBA@NiCH@CC to direct tube-furnace selenization at 350 °C under argon atmosphere. During the thermal transformation into selenide crystal phase, judicious combination and coordination of NiCH with NiFe-PBA facilitates the pore and defect formation. The morphology of the 3D interpenetrating nanoarchitectures is examined by field emission scanning electron microscopy (FESEM) and transmission electron microscopy (TEM). Figure 1b and Figure S2 (Supporting Information) show that NiCH possesses a densely interconnected hexagonal-like nanosheet structure that uniformly covers the carbon fiber surface. Higher magnification SEM image (Figure S3, Supporting Information) and TEM image (Figure 1g) further delineate the rough surface features of the NiCH nanosheets, which exhibit a lateral size of $\approx 4\text{--}5\ \mu\text{m}$ with a thickness of around $\approx 200\ \text{nm}$. As presented in Figure 1c,e,h and Figure S4 (Supporting Information), after the MOCCs crystallization, NiCH nanosheets are thoroughly surrounded by the uniformly crystallized NiFe-PBA nanocubes that have a narrow size distribution with an average particle size of 182 nm (Figure S5, Supporting Information). Each nanocube shares edge and/or corner with the adjacent nanocubes, resulting in the formation of interpenetrated continuous networks. This structural organization links up not only the nanocube crystals but also the NiCH nanosheets, thereby generating a tenaciously bridged and robust, yet flexible structure leveraging on the carbon fiber. Here, NiCH is exploited as a coordinative template to initiate the nucleation and growth of the MOCCs, as well as a defect generation medium in the course of the thermal decomposition. To corroborate the role of NiCH on the growth of MOCCs, the tendency of the NiFe-PBA nanocubes to be directly synthesized on the plain carbon fiber is investigated under the same conditions. As revealed in Figure S6 (Supporting Information), negligibly small amount of NiFe-PBA nanocubes poorly and sparsely decorate the carbon fiber surface, affirming the pivotal function of the NiCH on the assembly of the interpenetrating continuous networks.

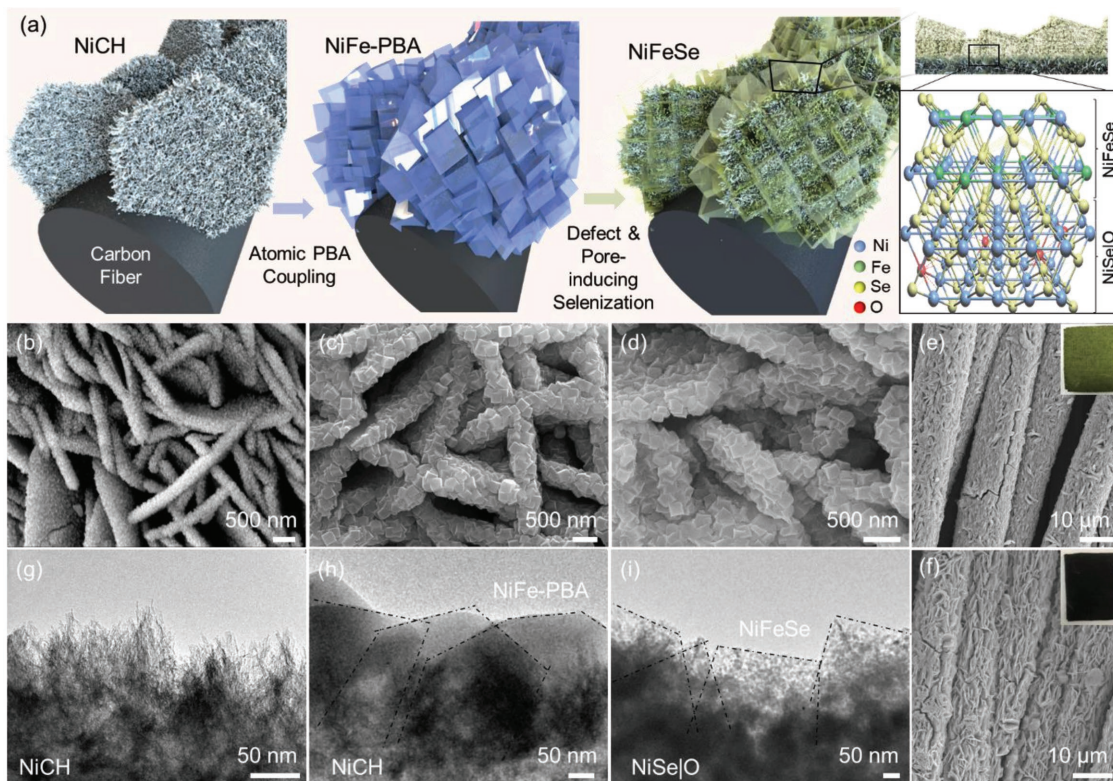


Figure 1. Synthetic route and morphological characterization of the NiCH@CC, NiFe-PBA@NiCH@CC, and NiFeSe@NiSe|O@CC. a) Schematic illustration for the synthesis strategy of the heterostructures. SEM images of the b) NiCH@CC, c) NiFe-PBA@NiCH@CC, and d) NiFeSe@NiSe|O@CC. Typical low-magnification SEM images of e) NiFe-PBA@NiCH@CC and f) NiFeSe@NiSe|O@CC showing the dense and uniform coverage on the carbon fiber. The insets show digital images of the corresponding materials. TEM images of g) NiCH@CC, h) NiFe-PBA@NiCH@CC, and i) NiFeSe@NiSe|O@CC. The black dashed lines serve as guide to distinguish the cubes.

Importantly, this approach is applicable to the synthesis of other MOCCs networks by taking the advantage of the as-grown carbonate hydroxide layer. ZIF-67 nanospheres and cobalt-iron PBA (CoFe-PBA) nanocubes are also successfully synthesized on cobalt carbonate hydroxide (CoCH) nanosheets to form ZIF-67@CoCH@CC and CoFe-PBA@CoCH@CC networks, respectively, (Figures S7 and S8, Supporting Information) similar to the NiFe-PBA@NiCH@CC. Fourier-transform infrared (FT-IR) and time evaluation studies further confirm that the metal ions in the carbonate hydroxide provides nucleation and growth sites for the MOCCs (Figures S9–S11, Supporting Information). After thermal selenization process, compared to the NiFe-PBA@NiCH@CC, the resulting NiFeSe@NiSe|O@CC becomes a highly porous hierarchical heterostructure, yet maintains the initial integration of the nanoparticles (Figure 1d,f,i and Figure S12, Supporting Information), confirming its structural robustness by means of the rational chemical decoupling between the carbonate hydroxide template and MOCCs.

Crystallinity and phase structures of the NiCH@CC, NiFe-PBA@NiCH@CC, and NiFeSe@NiSe|O@CC are studied by X-ray diffraction (XRD) analysis (Figure 2a). All diffraction peaks detected in the XRD spectrum of NiCH@CC match well with the monoclinic nickel carbonate hydroxide phase (shown by squares), $\text{Ni}_2\text{CO}_3(\text{OH})_2$ (JCPDS no: 35-0501), except the ones that are indexed to characteristic carbon fiber peaks at $2\theta = 25.7$ and 43.6° (shown by asterisks).^[9] The XRD spectrum of the

NiFe-PBA@NiCH@CC exhibits additional peaks to that of NiCH at $2\theta = 17.4, 24.7,$ and 35.1° , which corresponds to (200), (220), and (400) planes of the nickel hexacyanoferrate PBA (shown by triangles) (JCPDS card no.86-0501), respectively, confirming the successful growth of the NiFe-PBA nanocubes on the NiCH nanosheets.^[10] After thermal selenization process, new XRD peaks emerge accompanied with the complete disappearance of the typical NiCH and NiFe-PBA peaks, suggesting complete transformation of the NiFe-PBA@NiCH@CC into a new crystal phase. The XRD pattern of NiFeSe@NiSe|O@CC reveals the formation of the hexagonal $\text{Ni}_{0.85}\text{Se}$ (JCPDS no: 18-0888) with the peaks located at $2\theta = 16.9, 33.7, 44.6, 50.8,$ and 60.2° , which can be indexed to the crystal planes of (001), (101), (102), (110), and (103), respectively (shown by filled spheres).^[11] Slight peak shift and peak intensity change are observed in the XRD pattern of NiFeSe@NiSe|O@CC compared to that of NiSe|O@CC prepared by direct selenization of NiCH@CC (Figure S13, Supporting Information). This is attributed to the coexistence of Ni and Fe atoms in the NiFe-PBA crystal and their synchronous phase transformation into the $\text{Ni}_{(0.85-x)}\text{Fe}_x\text{Se}$ phase, which induces only a slight change in the crystal structure of the hexagonal $\text{Ni}_{0.85}\text{Se}$ with the Fe incorporation due to their similar atomic radii. Notably, besides the $\text{Ni}_{(0.85-x)}\text{Fe}_x\text{Se}$ peaks, NiO_x diffraction peaks (shown by empty spheres) are also detected in the XRD pattern of NiFeSe@NiSe|O@CC, which can be ascribed to the high oxygen content

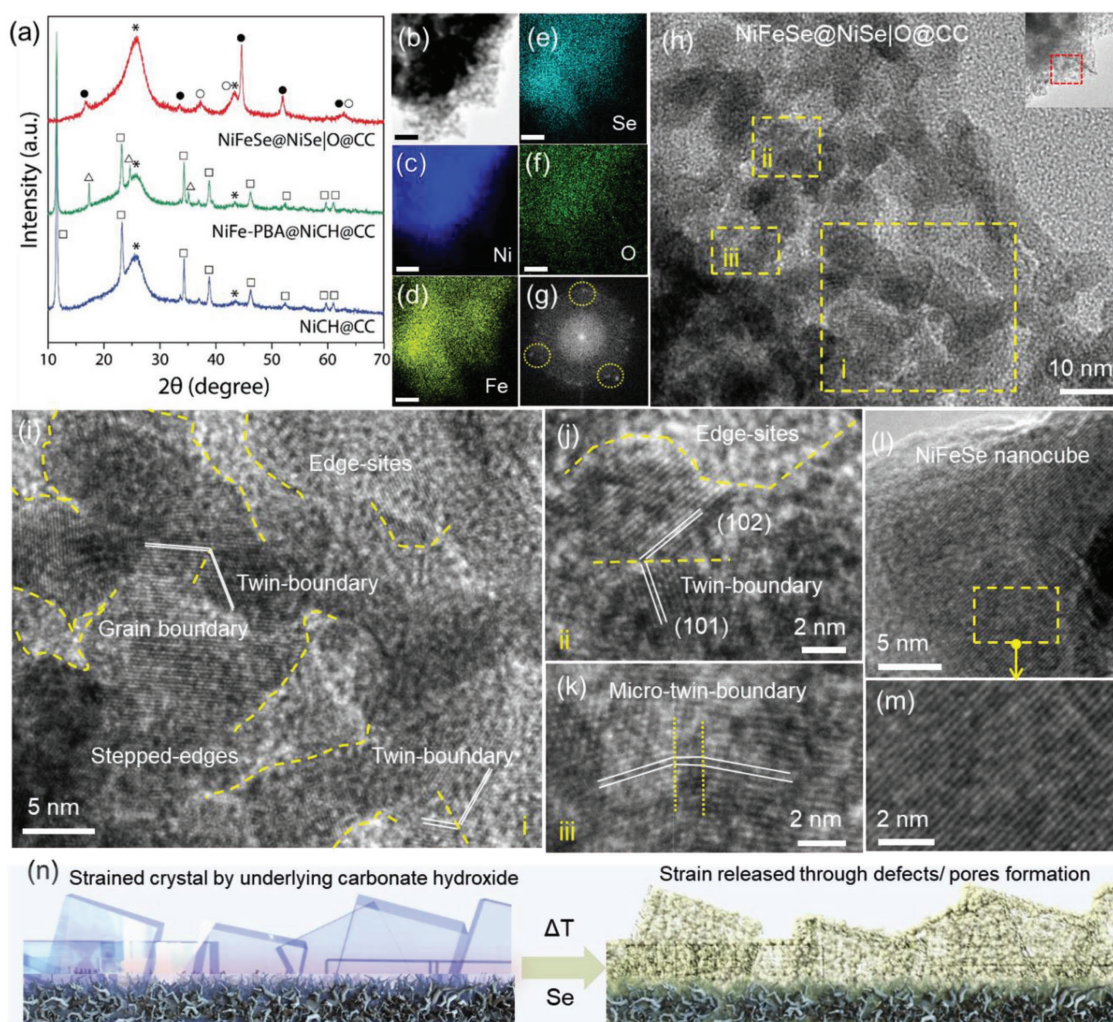


Figure 2. Characterization of the crystal structures. a) XRD patterns of the NiCH@CC, NiFe-PBA@NiCH@CC, and NiFeSe@NiSe|O@CC. b) HAADF-STEM image of the NiFeSe@NiSe|O@CC and the corresponding elemental mappings for c) Ni, d) Fe, e) Se, and f) O elements. The scale bar is 50 nm. g) FFT pattern of the HRTEM image in (j). h) Typical HRTEM image of the NiFeSe@NiSe|O@CC, which represents the red dashed square in the inset TEM image. i–k) HRTEM images representing the yellow dashed squares in (h). l, m) HRTEM images of the nearly defect-free discrete NiFeSe nanocubes, m) represents the yellow dashed square in (l). n) Schematic illustration for the formation process of the defective porous interconnected NiFeSe@NiSe|O@CC structure.

of the nickel carbonate hydroxide layer, rendering concurrent formation of the nickel selenide and oxide phase in the NiCH layer during the thermal treatment.^[12] The same diffraction peaks are also detected in the XRD pattern of the NiSe|O@CC, which suggests the formation of the oxide phase mostly in the support carbonate hydroxide derived selenide structure. Moreover, to gain insight into the surface electronic and chemical states of the elements in the NiFeSe@NiSe|O@CC, X-ray photoemission spectroscopy (XPS) analysis is employed (Figure S14, Supporting Information). High-resolution Ni 2p core-level spectrum is deconvoluted into two pairs of spin-orbit doublets originating from Ni²⁺ and Ni³⁺, revealing the coexistence of Ni²⁺ and Ni³⁺ species in the NiFeSe@NiSe|O@CC. The corresponding peak positions are close to that of the nickel-based selenides (Ni_(0.85–x)M_xSe, where M: metal) and signify the formation of metal–selenide bonds.^[11,13] In addition, one extra pair of peaks observed for NiO supports the as-detected nickel

oxide phase in the XRD analysis. Similar to the Ni 2p spectrum, the Fe 2p core-level spectrum shows coexistence of +2 and +3 valences, in which the binding energies are close to selenide-bonded iron, suggesting the co-occupancy of the nickel and iron atoms in the selenide structure.^[14] As for the Se 3d spectrum, two major peaks located at 54.4 and 55.9 eV are ascribed to the Se 3d_{5/2} and Se 3d_{3/2} region of metal–selenides, respectively.^[11b,14a] The survey scan XPS spectrum indicates that the NiFeSe@NiSe|O@CC is composed of Ni, Fe, Se, and O elements with a Ni/Fe atomic ratio of ≈1.4. Presence and homogenous distribution of the elements in the NiFeSe@NiSe|O@CC is further verified by TEM elemental mapping analysis (Figure 2b–f). The corresponding high-angle annular dark-field scanning transmission electron microscopy (HAADF-STEM) image in Figure 2b affirms the porous structure of the NiFeSe nanocubes on the NiSe|O layer. Based on the detailed SEM, XRD, XPS, and low-resolution TEM analysis, it is evident

that the NiFe-PBA nanocubes coordinated nickel carbonate hydroxide network is successfully converted into a porous NiFeSe@NiSe|O@CC crystal structure without structural collapse during the thermal selenization process. To further examine the porous nanostructure of the as-synthesized products in detail, high-resolution transmission electron microscopy (HRTEM) is conducted (Figure 2h–k, Figures S15 and S16, Supporting Information). Figure 2h reveals that NiFeSe@NiSe|O@CC is highly mesoporous consisting of numerous interconnected crystalline nanoparticles (5–10 nm) surrounded by pores. Higher magnification images taken from the arbitrarily selected regions of i, ii, and iii explicitly detail the nanocrystalline features in Figure 2i and Figure 2j,k, respectively. The NiFeSe@NiSe|O@CC nanostructure is rich in unsaturated sites in form of grain-boundaries and edge-sites, which transpire as interfacial boundaries established by nanocrystalline domains merged with adjacent ones or nanocrystalline domains bordered by pores, as presented by yellow dashed lines. Moreover, the nanostructure also encapsulates copious unsaturated sites as twin-boundary crystal defects that are identified over the entire crystal as evidenced by the fast Fourier transformation (FFT) in form of additional diffraction spots (Figure 2g). Figure 2j shows a typical lattice orientation of a twin-boundary, which manifests as a combination of (102) and (101)-oriented planes of the hexagonal NiFeSe crystal phase (Figure 2g). These types of lattice orientations evidently substantiate the formation of a highly unsaturated atomic site-concentrated NiFeSe@NiSe|O@CC structure. Notably, despite the defective porous nature, the crystallite nanograins are successively linked together through the boundaries without any noticeable gaps present, thereby consolidating electrical and mechanical contact of the overall structure. In contrast, the discrete NiFeSe nanocubes, prepared by selenization of discrete NiFe-PBA nanocubes (Figure S17, Supporting Information), exhibit a relatively regular atomic arrangement in the crystal lattice as presented in Figure 2l,m and Figure S18 (Supporting Information), signifying a nearly defect-free and less-porous crystal structure compared to NiFeSe@NiSe|O@CC. To corroborate the porous structure of the as-synthesized materials, nitrogen adsorption–desorption isotherms are obtained through sorption experiments (Figure S19 and Table S1, Supporting Information). NiFeSe@NiSe|O@CC exhibits a mixture of type-III and type-V sorption behavior with a notable hysteresis loop, confirming the presence of microporous and mesoporous structure, as also verified by the intense Barrett–Joyner–Halenda (BJH) pore size distribution peaks in the range of 2–12 nm.^[15] The Brunauer–Emmett–Teller (BET) surface area and BJH pore volume of the NiFeSe@NiSe|O@CC are determined to be 115.9 m² g⁻¹ and 0.121 cm³ g⁻¹, respectively. Notably, discrete NiFeSe nanocubes exhibit a significantly smaller BET surface area (26.3 m² g⁻¹) with a less-porous feature, as evidenced by the calculated small BJH pore volume of 0.06 cm³ g⁻¹. Formation of such a structurally distinct NiFeSe@NiSe|O@CC material with salient features is ascribed to the presence of the NiCH coordinative-template anchored to the NiFe-PBA nanocubes. First of all, the NiCH nanosheets confine the crystal growth of NiFe-PBA nanocubes and induce irregular arrangement of edge sharing nanocubes (Figure 1c,h) that is anticipated to contain greater number of crystal defects

than that of the template-free grown discrete NiFe-PBA nanocubes. Moreover, the selenization process promotes an unprecedented porous atomic reconstruction and departure from the ideal defect-free structure owing to dehydroxylation and decarboxylation of carbonate hydroxide during the thermal decomposition.^[16] In the course of gas release, pore formation occurs with generation of subtle distortion and high stress in the crystal structure in which unsaturated sites transpire inevitably, emerging as edge defects at hole sites, and grain and twin-boundaries at discontinuous fringe sites (Figure 2n).^[13,17] Thus, the NiFeSe@NiSe|O@CC structure not only displays an interconnected porous conductive network at the microscopic level, but also expose large fraction of reactive crystal boundaries elaborated with great number of unsaturated sites at the edges and interfaces at the atomic level. Such a judicious design of 3D molecular accessibility with porous interior, arranged interconnectivity and engineered defects makes it a potential candidate as a high-performance electrocatalyst.^[18]

The electrocatalytic activity of the NiFeSe@NiSe|O@CC toward HER and OER is investigated in 1 M aqueous KOH using typical three-electrode set-up. The HER and OER performances of the NiCH@CC and NiFePBA@NiCH@CC, as pristine samples (Figure S20, Supporting Information), discrete NiFeSe nanocubes and NiSe|O@CC network, as selenization products, and Pt/C@CC and RuO₂@CC, as the benchmark electrocatalysts, are evaluated for comparison. **Figure 3a** shows the polarization curves obtained from liner sweep voltammetry (LSV) measurements. NiFeSe@NiSe|O@CC exhibits a promising electrocatalytic HER activity comparable to that of Pt/C@CC. It can readily reach a geometrical current density (*j*) of -10 mA cm⁻² at a very low overpotential (η_{-10}) of 62 mV, which is slightly larger than that of the precious Pt/C@CC (32.6 mV at η_{-10}), but substantially surpasses the overpotential values of NiCH@CC (463 mV) and NiFePBA@NiCH@CC (>500 mV) at the same current density. In comparison, η_{-10} of the selenized samples, namely NiFeSe nanocubes and NiSe|O@CC electrocatalysts are 290 and 490 mV, respectively, which reveals that remarkable electrocatalytic HER activity is attained in NiFeSe@NiSe|O@CC through intact coordination and rational unsaturated site- and pore-inducing MOCCs crystallization and selenization process. The HER kinetics of the electrocatalysts is studied over their corresponding Tafel plots derived from the polarization curves by plotting overpotential (η) against log (*j*) (Figure 3b and Figure S20 inset, Supporting Information). The NiFeSe@NiSe|O@CC possesses a remarkably smaller Tafel slope of 48.9 mV dec⁻¹ compared to 472, 130, 256, and 94 mV dec⁻¹ obtained for NiCH@CC, NiFePBA@NiCH@CC, NiFeSe nanocubes, and NiSe|O@CC, respectively, indicating its favorable reaction kinetics toward hydrogen evolution. Notably, the HER performance of the NiFeSe@NiSe|O@CC is superior or comparable to that of the Pt/C@CC (41.2 mV dec⁻¹) and recently reported selenide-based HER electrocatalysts (see Table S2 in the Supporting Information for the detailed comparison). Besides the overpotential and Tafel slope, long-term stability is another important parameter for judgment of the intrinsic performance of an electrocatalyst. The durability of the electrocatalysts is examined for 50 h at a constant applied overpotential, corresponding to an initial current density of -10 mA cm⁻². As presented in Figure 3c, during the tests, the

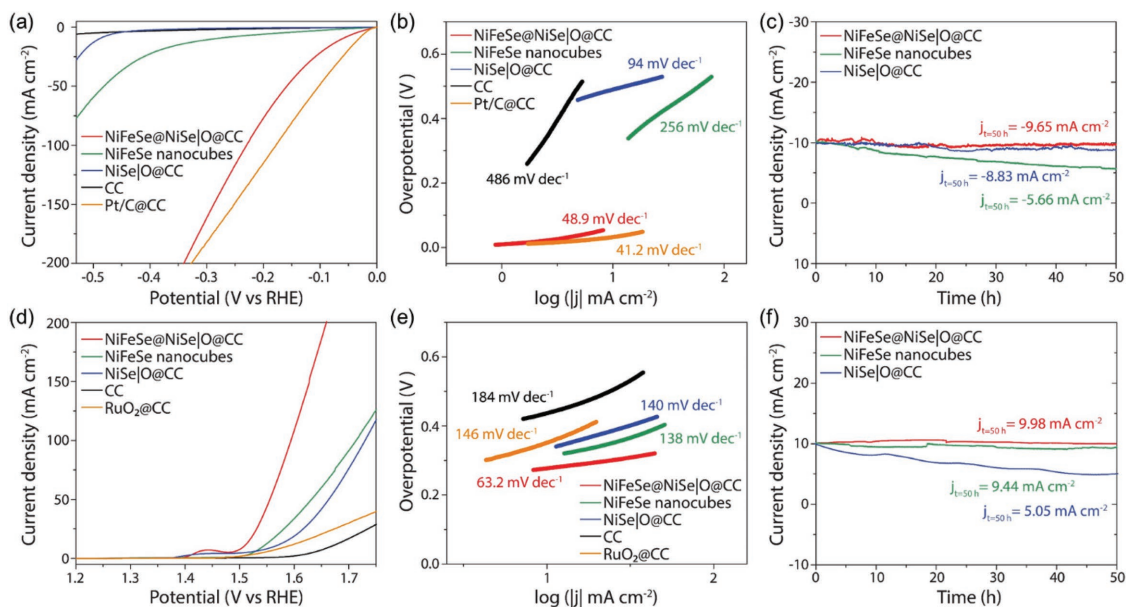


Figure 3. Electrochemical HER and OER performances of the NiFeSe@NiSe|O@CC along with the NiFeSe nanocubes, NiSe|O@CC, CC, Pt/C@CC, and RuO₂@CC for comparison. a) HER polarization curves recorded at a scan rate of 5 mV s⁻¹ in 1 M KOH. b) Corresponding Tafel plots of the electrocatalysts in (a). c) Time dependence of current density under static overpotential showing the durability of the electrocatalysts over 50 h. d) OER polarization curves recorded at a scan rate of 0.5 mV s⁻¹ in 1 M KOH. e) Corresponding Tafel plots of the electrocatalysts in (d). f) Time dependence of current density under static overpotential showing the durability of the electrocatalysts over 50 h.

current density maintains almost unchanged for NiFeSe@NiSe|O@CC, while degradation is observed for NiFeSe nanocubes and NiSe|O@CC to -5.66 and -8.83 mA cm⁻², respectively. The negligible decay of the NiFeSe@NiSe|O@CC electrocatalyst after 50 h continuous HER operation indicates its superior stability in the long-term electrochemical process (Figure S21, Supporting Information). This can be ascribed to the interconnected, porous, and defective structure, which can efficiently alleviate the mechanical distortion during the hydrogen bubble evolution and tolerate the intense gas generation, hence avoiding any damage and disintegration in the course of reaction.^[4b,17b,d] XRD, SEM, and HRTEM studies of the NiFeSe@NiSe|O@CC after stability measurement further corroborate the well-retained crystallographic phase with the intact micro and nanostructural properties elaborated with pores and defects (Figures S22 and S23, Supporting Information). OER activity of the electrocatalysts is also investigated in the same set-up using 1.0 M KOH. The polarization curves (Figure 3d) show that NiFeSe@NiSe|O@CC has a better OER activity than that of NiFeSe nanocubes and NiSe|O@CC, as in the case of HER. The overpotential to drive current densities of 10, 20, and 100 mA cm⁻² are only 270, 290, and 360 mV, respectively, which is comparable to or outperforms RuO₂@CC (350 mV) and other recently reported selenide-based electrocatalysts (see Table S3 in the Supporting Information for the detailed comparison). Meanwhile, η_{10} of the NiFeSe@NiSe|O@CC is ≈ 40 , 60, 80, 120, and 130 mV smaller than that of the NiFeSe nanocubes, NiSe|O@CC, NiFePBA@NiCH@CC, RuO₂@CC, and NiCH@CC, respectively. Moreover, NiFeSe@NiSe|O@CC possesses a more favorable OER kinetics with a small Tafel slope of 63.2 mV dec⁻¹, which is the lowest among the other candidates (RuO₂@CC (146 mV dec⁻¹), NiFeSe nanocubes

(138 mV dec⁻¹), NiSe|O@CC (140 mV dec⁻¹), NiFePBA@NiCH@CC (220 mV dec⁻¹), NiCH@CC (180 mV dec⁻¹)) (Figure 3e). Chronoamperometric test (Figure 3f) also shows that NiFeSe@NiSe|O@CC is reasonably stable and able to maintain the corresponding initial current density with only a slight decrease from 10 to 9.98 mA cm⁻² after 50 h of unceasing operation (Figure S24, Supporting Information).

To attain deeper understanding on the distinct performances of the catalysts, their intrinsic electrocatalytic properties are assessed in detail by examining electrochemically active surface areas (ECSAs), hydrogen/oxygen turnover frequencies (TOFs) and electrochemical impedance characteristics. Double-layer capacitances (C_{dl}) of the electrocatalysts are obtained from cyclic voltammetry measurements to assess the ECSAs (Figure S25, Supporting Information). As presented in Figure 4a,b, the NiFeSe@NiSe|O@CC possesses the largest active surface area with a C_{dl} of ≈ 44 mF cm⁻², which is more than two and four times larger than that of the NiFeSe nanocubes and NiSe|O@CC, respectively. This can be ascribed to the porous and defect-rich NiFeSe@NiSe|O@CC structure that renders the catalyst with more exposed active centers, further corroborating its promising HER and OER activities. Besides the number of active sites, activity level of these sites toward the desired electrocatalytic reaction plays a crucial role in determining the overall catalytic performance. To characterize the activity level of the catalysts, the rate of hydrogen/oxygen evolution per surface site for each catalyst is calculated and expressed as TOF. At an overpotential of 100 mV for HER (Figure 4c), the TOF value reaches a maximum (1.54 H₂ s⁻¹) for the NiFeSe@NiSe|O@CC, which is almost 4 and 14 times that of the NiFeSe nanocubes (0.395 H₂ s⁻¹) and NiSe|O@CC (0.112 H₂ s⁻¹), respectively, further indicating the high intrinsic activity of

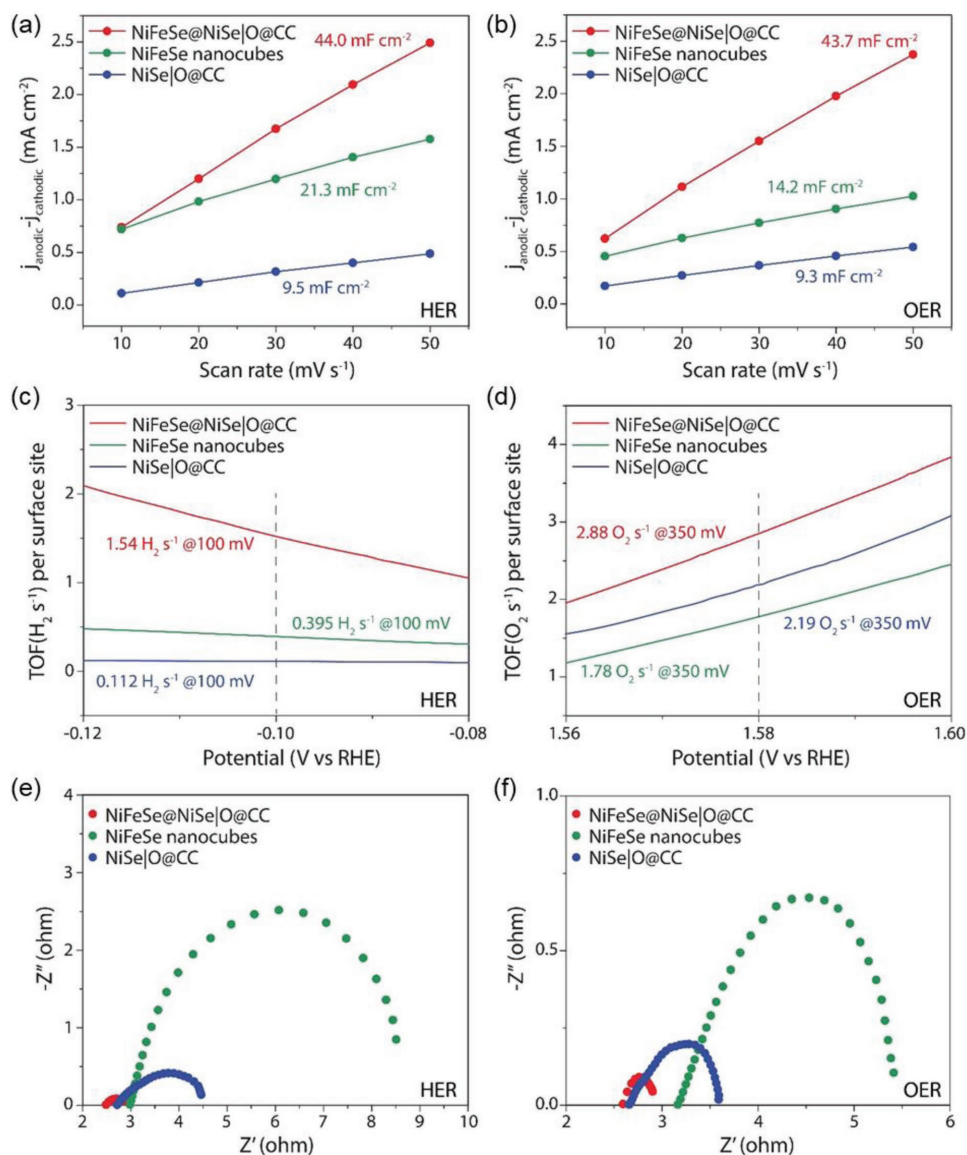


Figure 4. Investigation of the intrinsic electrocatalytic properties of the NiFeSe@NiSe|O@CC, NiFeSe nanocubes, and NiSe|O@CC. Estimation of the double layer capacitances using the capacitive current densities for a) HER at 0.05 V (vs RHE) and b) OER at 1.05 V (vs RHE) as a function of scan rate. c) H₂ and d) O₂ turnover frequencies per surface site. EIS Nyquist plots for e) HER at -0.2 V (vs RHE) and f) OER at 1.6 V (vs RHE).

NiFeSe@NiSe|O@CC. Furthermore, in the potential range of OER, at an overpotential of 350 mV (Figure 4d), the calculated TOFs are 2.88 (NiFeSe@NiSe|O@CC), 2.19 (NiSe|O@CC), and 1.78 O₂ s⁻¹ (NiFeSe nanocubes). It should be noted that, compared to TOFs calculated for HER, the order of magnitude improvement is smaller in the TOFs calculated for OER, although similar ECSA values are obtained for both hydrogen and oxygen evolution reactions (Figure 4a,b). To gain insight into this discrepancy, surface electronic structure of the NiFeSe@NiSe|O@CC after HER and OER tests is investigated through XPS analysis since surface compositional change during the electrochemical reactions could lead in situ formation of active sites.^[19] After OER test, the Ni 2p core-level XPS spectrum exhibits four peaks representing the Ni²⁺ 2p^{3/2}, Ni²⁺ 2p^{1/2}, Ni³⁺ 2p^{3/2}, and Ni³⁺ 2p^{1/2} binding energies at peak positions similar

to that of the as-prepared NiFeSe@NiSe|O@CC (Figure S26, Supporting Information). Meanwhile, new peaks are detected at 857.9 and 877.6 eV, which suggests the formation of oxyhydroxide phase.^[14a] Similarly, Fe 2p XPS spectrum manifests slight oxidation of Fe²⁺ valence into Fe³⁺ during the OER process as revealed by the intensity increase in Fe³⁺ peak, further affirming the phase transformation into iron oxyhydroxide. Consistently, unlike the as-prepared NiFeSe@NiSe|O@CC, O 1s spectrum of post-OER catalyst also reveals a peak at 530.9 eV related to the binding energy of -OH groups.^[20] The XPS investigations of post-OER catalyst obviously show that surface selenide phase is partly transformed into oxyhydroxide phase, unveiling a surface composition change under the oxidative conditions of OER. Note that surface-bound oxyhydroxides show superior electrocatalytic OER activity compared to metal

chalcogenides and phosphides.^[19,21] Thus, it is anticipated that in situ generated oxyhydroxides throughout the OER endow the catalyst with active sites that might not be well accounted by ECSAs since it is calculated in a small potential range with mostly dominated by double layer capacitance effects, which elucidates the less significant TOFs difference among the OER electrocatalysts. Meanwhile, XPS analysis of NiFeSe@NiSe|O@CC after HER test (Figure S27, Supporting Information) indicates no obvious change in the surface chemical composition, suggesting that the real HER active sites are defective sites, whose permanence is corroborated by the HRTEM of postcatalytic sample (Figure S23, Supporting Information). Moreover, high activity of NiFeSe@NiSe|O@CC, compared to that of NiFeSe nanocubes and NiSe|O@CC, can be also attributed to its better conductivity as verified by electrochemical impedance spectroscopy (EIS) (Figure 4e,f). Nyquist plots show that it possesses a lower charge transfer resistance and contact resistance,

which is mainly owing to the unique 3D interconnected structural assembly that ensures excellent conductivity along the carbon fiber surface to the NiFeSe@NiSe|O@CC and efficient electron transfer kinetics during the electrocatalytic reactions.

Considering the encouraging HER and OER performances of the NiFeSe@NiSe|O@CC, it is anticipated that the NiFeSe@NiSe|O@CC can serve as an efficient bifunctional electrocatalyst for overall water splitting in alkaline media. Accordingly, an electrolyzer is further assembled by integrating the NiFeSe@NiSe|O@CC electrodes as both anode and cathode in 1 M KOH. **Figure 5a** presents the overall water splitting activity of two-electrode system. Remarkably, NiFeSe@NiSe|O@CC exhibits an impressive catalytic activity as reflected by the small cell voltage requirement of 1.56 V to attain a current density of 10 mA cm⁻², which exceeds most of the previously reported bifunctional electrocatalysts such as transition metal phosphides, chalcogenides, oxides, and hydroxides (see Table S4 in

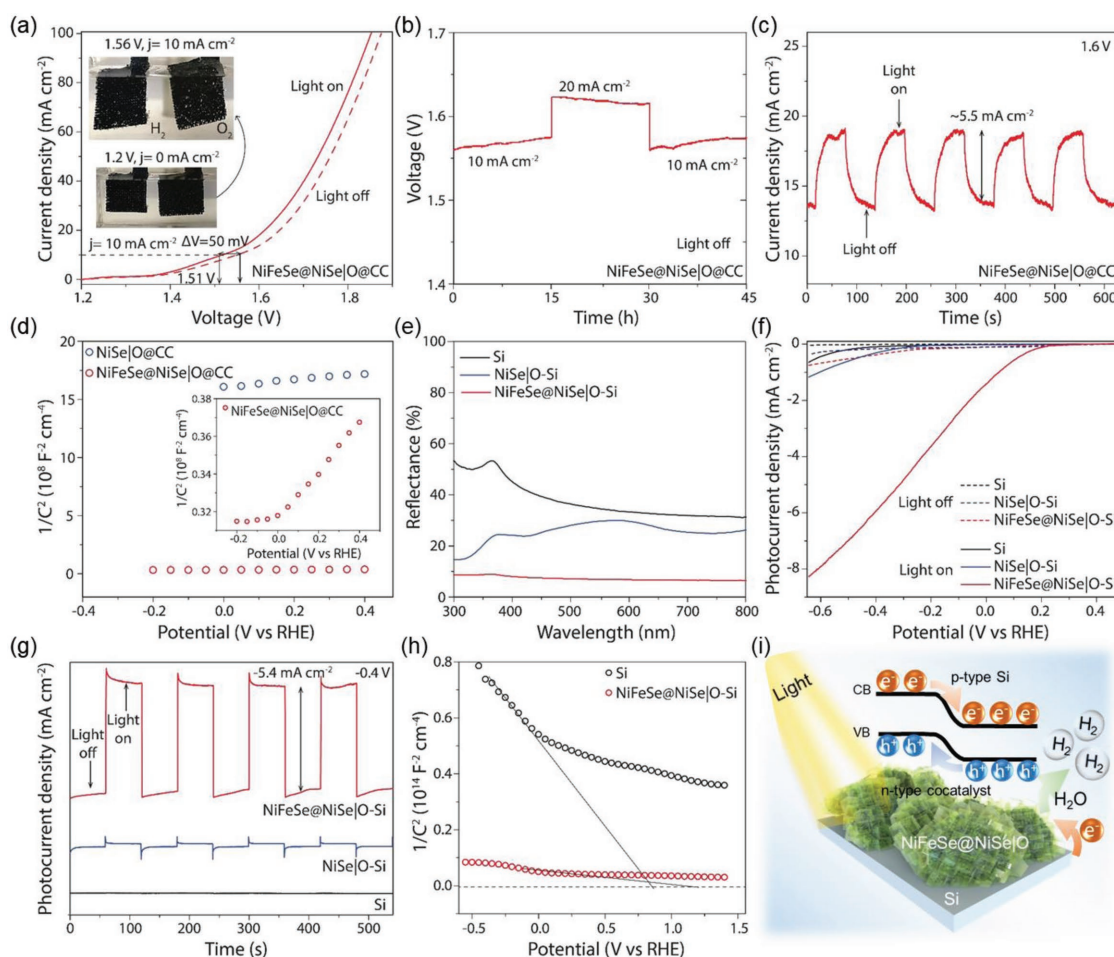


Figure 5. Electrochemical and photo-electrochemical water splitting performance of the NiFeSe@NiSe|O@CC. a) Polarization curves obtained in two-electrode configuration using the NiFeSe@NiSe|O@CC as both anode and cathode under dark (light off condition) and simulated one sun irradiation (100 mW cm⁻²) (light on condition). b) Time dependence of voltage under static current densities of 10 and 20 mA cm⁻² over 45 h of continuous operation for the NiFeSe@NiSe|O@CC cell. c) Chronoamperometric *i*-*t* curve of the NiFeSe@NiSe|O@CC cell at a bias voltage of 1.6 V under chopped illumination. d) Mott-Schottky plots of the NiFeSe@NiSe|O@CC and NiSe|O@CC. e) UV-vis DRS spectra of the Si, NiSe|O-Si, and NiFeSe@NiSe|O-Si photocathodes under dark and simulated one sun irradiation (100 mW cm⁻²). g) Chronoamperometric *i*-*t* curve of the Si, NiSe|O-Si, and NiFeSe@NiSe|O-Si at a bias potential of -0.4 V (vs RHE) under chopped illumination. h) Mott-Schottky plots of the Si and NiFeSe@NiSe|O-Si. i) Schematic illustration for the proposed PEC mechanism of the NiFeSe@NiSe|O-Si structure.

the Supporting Information for the detailed comparison).^[13,22] Vigorously generated hydrogen and oxygen bubbles at 1.56 V can be observed on the anode and cathode as presented in the inset of Figure 5a. Furthermore, long-term electrochemical stability of the NiFeSe@NiSe|O@CC is examined by chronopotentiometric measurements by applying consecutive current densities of 10, 20, and 10 mA cm⁻², and investigating the changes in the initial resulting potentials during 45 h of continuous electrolysis (Figure 5b). The NiFeSe@NiSe|O@CC possesses a good long-term stability for overall water splitting, unveiling that it is not only a highly active, but also a very stable bifunctional electrocatalyst. Moreover, apart from the sole electrocatalytic activity of the NiFeSe@NiSe|O@CC, its light-induced electrocatalytic performance is also studied. Recent studies have well demonstrated that light irradiation could effectively boost the electrocatalytic HER and OER activities through various strategies such as generation of active sites via interaction of plasmon-excited hot electrons or photogenerated carriers with the electrocatalyst, and/or lowering the activation energy of the electrocatalytic reaction via photothermic effect.^[23] To investigate the effect of light-irradiation on the overall water splitting, a comparative polarization curve is obtained by illuminating the electrodes with simulated one sun irradiation (100 mW cm⁻²). Upon exposure to irradiation (light on condition), voltage requirement of the cell to attain a desired current density is successfully lowered compared to light off condition (Figure 5a), suggesting its improved electrocatalytic performance with light. For example, irradiated NiFeSe@NiSe|O@CC can reach a current density of 10 mA cm⁻² at a cell voltage of 1.51 V, which is 50 mV smaller than that of the measured in the dark. To gain more insight into the effect of irradiation on the improved overall water splitting electrocatalytic performance, HER and OER performances of the NiFeSe@NiSe|O@CC are investigated using standard three-electrode set-up under simulated illumination (Figure S28, Supporting Information). Both HER and OER activities are facilitated when the NiFeSe@NiSe|O@CC is irradiated by the solar simulator. The improvement in HER activity can be attributed to the photogenerated electrons from excited nickel oxide, as suggested by the previous studies, which is analogous to the hot-electrons excited by the resonant photons.^[23a] Improved light absorption property of the wide bandgap (≈ 3.4 eV) nickel oxide with the combination of a good light harvesting material enhances its photoresponse.^[23a,24] Particularly, oxygen evolution reaction behavior of the NiFeSe@NiSe|O@CC is significantly affected by the irradiation as evidenced by the prompt and prominent increase in the peak area around 1.4–1.5 V, which suggests the intense oxidation of nickel–iron species.^[23a] Based on the previous discussion, in situ generated oxyhydroxides are the main active sites in OER, thus generation of these species leads further increase in the OER activity. The results suggest that overall water splitting activity is triggered by the photogenerated electrons from excited NiO, which subsequently draws electrons from NiFeSe site and induces photogenerated holes, promoting the oxidation of nickel and iron to oxyhydroxide phase.^[23a] Thus, it leads to a synchronous improvement in HER and OER activity, thereby directly affecting the overall water splitting performance. To corroborate the photoresponse of the NiFeSe@NiSe|O@CC, chronoamperometric *i*-*t* curve under

chopped illumination is obtained. As shown in Figure 5c, the electrolysis cell generates a rapid and continuous photoresponse with a photogenerated current density of 5.5 mA cm⁻² at 1.6 V bias upon each repeated on-off cycle under simulated one sun irradiation, confirming light-induced catalytic activity of the NiFeSe@NiSe|O@CC in accordance with the polarization curves in Figure 5a. The UV–vis absorption spectroscopy further reveals the good light-harvesting properties of the samples (Figure S29, Supporting Information). Moreover, Kubelka–Munk plot obtained using the UV–vis diffusive reflectance spectrum (DRS) manifests the small bandgap of the NiFeSe@NiSe|O@CC (Figure S30, Supporting Information). Inspired by the promising light harvesting nature and small bandgap of the NiFeSe@NiSe|O@CC, semiconductor property of the catalyst is further examined by Mott–Schottky plots. As presented in Figure 5d, the positive slopes of the Mott–Schottky plots indicate n-type semiconductor property of the NiFeSe@NiSe|O@CC and NiSe|O@CC. Impressive HER performance, n-type semiconductor property and good light-harvesting ability of NiFeSe@NiSe|O@CC could also make it an effective cocatalyst and type-II heterojunction candidate when combined with p-type silicon (Si) as a photocathode material for PEC water splitting (Figure 5e). To prove this proposition, PEC performances of Si, NiSe|O-Si, and NiFeSe@NiSe|O-Si are evaluated by collecting polarization curves under simulated solar irradiation (Figure 5f). The delivered photocurrent densities of all the samples under light off condition are negligible as seen from Figure 5f. Upon illumination, compared to the slight improvement in the PEC activity of NiSe|O-Si and bare Si, NiFeSe@NiSe|O-Si exhibits a significant shift in the onset overpotential and a prominent increase in the delivered photocurrent density. For example, NiFeSe@NiSe|O-Si achieves an onset potential of 0.22 V, which is higher than that of the recently reported similar photocathode materials such as MSi/H-Co_{0.85}Se|P and MSi/EG/Ni₃Se₂/Co₉S₈.^[22b,25] *i*-*t* curves of Si, NiSe|O-Si, and NiFeSe@NiSe|O-Si, obtained under chopped illumination at an applied bias potential of -0.4 V (Figure 5g), further manifests the remarkable photocurrent density improvement, confirming that NiFeSe@NiSe|O effectively boosts the PEC performance of Si. To investigate intrinsic photo-electrocatalytic properties of NiFeSe@NiSe|O-Si, flat band potential and charge carrier density are evaluated through the Mott–Schottky analysis. Based on the Mott–Schottky plots in Figure 5h, NiFeSe@NiSe|O-Si shows a much smaller slope than that of the Si, suggesting an increase in charge carrier density, thus indicating the intense utilization of the solar energy. The NiFeSe@NiSe|O-Si electrode also exhibits a more positive flat band potential compared to bare Si. This reveals a higher degree of band bending at the semiconductor/electrolyte interface, and thus improved charge separation and better water reduction kinetics.^[26] Electrochemical impedance measurements further verify the enhanced carrier transport of NiFeSe@NiSe|O-Si through smaller charge transfer resistance (Figure S31, Supporting Information). These results explicitly reveal that the poor intrinsic solar-driven hydrogen generation activity of bare Si can be significantly enhanced via constructing NiFeSe@NiSe|O-Si (Figure 5i). This can be attributed to structural and intrinsic engineering of the photocathode material. First, enhanced light-harvesting ability of NiFeSe@NiSe|O-Si

warrants the effectual utilization of incoming light. Moreover, the n-type NiFeSe@NiSe|O on p-type Si establishes a typical type-II heterojunction, in which photogenerated electrons from Si can be rapidly transferred to the NiFeSe@NiSe|O with remarkably lessened photogenerated carrier recombination, and subsequently employed in HER.^[22b] In addition, impressive electrocatalytic HER activity of NiFeSe@NiSe|O makes it a promising cocatalyst, which can successfully extract the photogenerated charge carriers and decrease the overpotential requirement, thus promotes the proton reduction reaction.^[27] Considering the high cost of noble metal cocatalysts, it is valuable to design and fabricate such low-cost and noble metal free substitutes to further enhance the advance of photo-electrochemical hydrogen production.

3. Conclusions

In summary, a coordinative-template strategy featuring a crystallization process affords an intact confinement of the metal organic coordination compounds on a carbonate hydroxide template. Moreover, pseudomorphic transformation by selection of the interlocked bilayered structure allows porous atomic reconstruction and departure from the ideal defect-free structure via stress-inducing thermal decomposition of the underlying template. Eventually, the judicious design and transformation endow the 3D NiFeSe@NiSe|O@CC interpenetrating structure with unsaturated atomic sites, porous morphology, high conductivity, and high surface area, which are beneficial for electrocatalytic performance. When employed as an electrocatalyst electrode, the NiFeSe@NiSe|O@CC exhibits outstanding electrochemical performance toward HER and OER in alkaline media with low overpotentials and Tafel slopes. Accordingly, when employed in an alkaline electrolyzer, the NiFeSe@NiSe|O@CC also serves as an efficient bifunctional electrocatalyst for overall water splitting. In addition, when integrated with p-type Si for PEC water splitting, the NiFeSe@NiSe|O-Si can significantly enhance PEC hydrogen production performance. Importantly, the generality of the proposed coordinative-template strategy scheme is demonstrated for the preparation of other interconnected metal organic coordination compounds, which may be exploited for diverse potential applications in energy storage, conversion, or environmental purposes.

Supporting Information

Supporting Information is available from the Wiley Online Library or from the author.

Acknowledgements

This work was supported by Ministry of Education (MOE), Singapore under R-263-000-C85-112, and R-263-000-D08-114 grants.

Conflict of Interest

The authors declare no conflict of interest.

Keywords

electrochemical and PEC water splitting, metal-organic, MOF, PBA

Received: September 25, 2018

Revised: October 23, 2018

Published online: November 8, 2018

- [1] a) Y. Liu, X. Hua, C. Xiao, T. Zhou, P. Huang, Z. Guo, B. Pan, Y. Xie, *J. Am. Chem. Soc.* **2016**, *138*, 5087; b) D. Yan, Y. Li, J. Huo, R. Chen, L. Dai, S. Wang, *Adv. Mater.* **2017**, *29*, 1606459; c) X. Fan, Y. Liu, S. Chen, J. Shi, J. Wang, A. Fan, W. Zan, S. Li, W. A. Goddard, X.-M. Zhang, *Nat. Commun.* **2018**, *9*, 1809; d) Y. Yin, J. Han, Y. Zhang, X. Zhang, P. Xu, Q. Yuan, L. Samad, X. Wang, Y. Wang, Z. Zhang, *J. Am. Chem. Soc.* **2016**, *138*, 7965.
- [2] a) X. Yu, P. Han, Z. Wei, L. Huang, Z. Gu, S. Peng, J. Ma, G. Zheng, *Joule* **2018**, *2*, 1610; b) T. Y. Ma, Y. Zheng, S. Dai, M. Jaroniec, S. Z. Qiao, *J. Mater. Chem. A* **2014**, *2*, 8676; c) J. Duan, S. Chen, M. Jaroniec, S. Z. Qiao, *ACS Catal.* **2015**, *5*, 5207.
- [3] a) M. Q. Yang, J. Wang, H. Wu, G. W. Ho, *Small* **2018**, *14*, 1703323; b) H. A. Tahini, X. Tan, U. Schwingenschlöggl, S. C. Smith, *ACS Catal.* **2016**, *6*, 5565; c) X. Cheng, E. Fabbri, M. Nachtegaal, I. E. Castelli, M. El Kazzi, R. Haumont, N. Marzari, T. J. Schmidt, *Chem. Mater.* **2015**, *27*, 7662.
- [4] a) G. Yilmaz, C. F. Tan, M. Hong, G. W. Ho, *Adv. Funct. Mater.* **2018**, *28*, 1704177; b) H. Wang, H.-W. Lee, Y. Deng, Z. Lu, P.-C. Hsu, Y. Liu, D. Lin, Y. Cui, *Nat. Commun.* **2015**, *6*, 7261; c) G. Liu, W. Li, R. Bi, C. Atangana Etogo, X.-Y. Yu, L. Zhang, *ACS Catal.* **2018**, *8*, 1720.
- [5] a) E. J. Crossland, N. Noel, V. Sivaram, T. Leijtens, J. A. Alexander-Webber, H. J. Snaith, *Nature* **2013**, *495*, 215; b) K. Shen, L. Zhang, X. Chen, L. Liu, D. Zhang, Y. Han, J. Chen, J. Long, R. Luque, Y. Li, *Science* **2018**, *359*, 206; c) X. Cui, Z. Pan, L. Zhang, H. Peng, G. Zheng, *Adv. Energy Mater.* **2017**, *7*, 1701456.
- [6] a) Y. Zhao, B. Jin, Y. Zheng, H. Jin, Y. Jiao, S. Z. Qiao, *Adv. Energy Mater.* **2018**, *8*, 1801926; b) H. Jin, C. Guo, X. Liu, J. Liu, A. Vasileff, Y. Jiao, Y. Zheng, S.-Z. Qiao, *Chem. Rev.* **2018**, *118*, 6337; c) J. Liu, Y. Zheng, Z. Wang, Z. Lu, A. Vasileff, S.-Z. Qiao, *Chem. Commun.* **2018**, *54*, 463.
- [7] J. Liu, D. Zhu, Y. Zheng, A. Vasileff, S.-Z. Qiao, *ACS Catal.* **2018**, *8*, 6707.
- [8] J. Jiang, J. Liu, X. Huang, Y. Li, R. Ding, X. Ji, Y. Hu, Q. Chi, Z. Zhu, *Cryst. Growth Des.* **2009**, *10*, 70.
- [9] a) D. Lee, Q. X. Xia, J. M. Yun, K. H. Kim, *Appl. Surf. Sci.* **2018**, *433*, 16; b) G. Zhang, S. Hou, H. Zhang, W. Zeng, F. Yan, C. C. Li, H. Duan, *Adv. Mater.* **2015**, *27*, 2400.
- [10] M. Hu, S. Ishihara, K. Ariga, M. Imura, Y. Yamauchi, *Chem. - Eur. J.* **2013**, *19*, 1882.
- [11] a) H. Peng, C. Wei, K. Wang, T. Meng, G. Ma, Z. Lei, X. Gong, *ACS Appl. Mater. Interfaces* **2017**, *9*, 17067; b) L. Du, W. Du, H. Ren, N. Wang, Z. Yao, X. Shi, B. Zhang, J. Zai, X. Qian, *J. Mater. Chem. A* **2017**, *5*, 22527.
- [12] Z. Liu, A. Zhu, F. Cai, L. Tao, Y. Zhou, Z. Zhao, Q. Chen, Y.-B. Cheng, H. Zhou, *J. Mater. Chem. A* **2017**, *5*, 6597.
- [13] C. Hu, L. Zhang, Z. J. Zhao, A. Li, X. Chang, J. Gong, *Adv. Mater.* **2018**, *30*, 1705538.
- [14] a) Z. Wang, J. Li, X. Tian, X. Wang, Y. Yu, K. A. Owusu, L. He, L. Mai, *ACS Appl. Mater. Interfaces* **2016**, *8*, 19386; b) L. Lv, Z. Li, K.-H. Xue, Y. Ruan, X. Ao, H. Wan, X. Miao, B. Zhang, J. Jiang, C. Wang, *Nano Energy* **2018**, *47*, 275.
- [15] M. Thommes, K. Kaneko, A. V. Neimark, J. P. Olivier, F. Rodriguez-Reinoso, J. Rouquerol, K. S. Sing, *Pure Appl. Chem.* **2015**, *87*, 1051.

- [16] a) N. Kanari, D. Mishra, I. Gaballah, B. Dupré, *Thermochim. Acta* **2004**, *410*, 93; b) J. Pérez-Ramírez, G. Mul, F. Kapteijn, J. A. Moulijn, *J. Mater. Chem.* **2001**, *11*, 821.
- [17] a) J. Wang, Z. Zeng, C. R. Weinberger, Z. Zhang, T. Zhu, S. X. Mao, *Nat. Mater.* **2015**, *14*, 594; b) S. Zhao, M. Li, M. Han, D. Xu, J. Yang, Y. Lin, N. E. Shi, Y. Lu, R. Yang, B. Liu, *Adv. Funct. Mater.* **2018**, *28*, 1706018; c) Y. Wang, L. Tao, Z. Xiao, R. Chen, Z. Jiang, S. Wang, *Adv. Funct. Mater.* **2018**, *28*, 1705356; d) Y. Yan, L. Thia, B. Y. Xia, X. Ge, Z. Liu, A. Fisher, X. Wang, *Adv. Sci.* **2015**, *2*, 1500120.
- [18] G. Yilmaz, K. M. Yam, C. Zhang, H. J. Fan, G. W. Ho, *Adv. Mater.* **2017**, *29*, 1606814.
- [19] a) X. Xu, F. Song, X. Hu, *Nat. Commun.* **2016**, *7*, 12324; b) H. Liang, A. N. Gandhi, C. Xia, M. N. Hedhili, D. H. Anjum, U. Schwingenschlöggl, H. N. Alshareef, *ACS Energy Lett.* **2017**, *2*, 1035.
- [20] C. Xia, Q. Jiang, C. Zhao, M. N. Hedhili, H. N. Alshareef, *Adv. Mater.* **2016**, *28*, 77.
- [21] H. Liang, A. N. Gandhi, D. H. Anjum, X. Wang, U. Schwingenschlöggl, H. N. Alshareef, *Nano Lett.* **2016**, *16*, 7718.
- [22] a) H. Wu, X. Lu, G. Zheng, G. W. Ho, *Adv. Energy Mater.* **2018**, *8*, 1702704; b) Y. Hou, M. Qiu, G. Nam, M. G. Kim, T. Zhang, K. Liu, X. Zhuang, J. Cho, C. Yuan, X. Feng, *Nano Lett.* **2017**, *17*, 4202.
- [23] a) X. Han, Y. Yu, Y. Huang, D. Liu, B. Zhang, *ACS Catal.* **2017**, *7*, 6464; b) Y. Shi, J. Wang, C. Wang, T.-T. Zhai, W.-J. Bao, J.-J. Xu, X.-H. Xia, H.-Y. Chen, *J. Am. Chem. Soc.* **2015**, *137*, 7365; c) J. Wang, L. Zhu, G. Dharan, G. W. Ho, *J. Mater. Chem. A* **2017**, *5*, 16580.
- [24] Y. Yang, S. Niu, D. Han, T. Liu, G. Wang, Y. Li, *Adv. Energy Mater.* **2017**, *7*, 1700555.
- [25] Y. Hou, M. Qiu, T. Zhang, X. Zhuang, C. S. Kim, C. Yuan, X. Feng, *Adv. Mater.* **2017**, *29*, 1701589.
- [26] H. Zhang, Q. Ding, D. He, H. Liu, W. Liu, Z. Li, B. Yang, X. Zhang, L. Lei, S. Jin, *Energy Environ. Sci.* **2016**, *9*, 3113.
- [27] J. Yang, D. Wang, H. Han, C. Li, *Acc. Chem. Res.* **2013**, *46*, 1900.